This article has been accepted for publication in IEEE Sensors Journal. This is the author's version which has not been fully edited and content may change prior to final publication. Citation information: DOI 10.1109/JSEN.2023.3327547

Tattoo-like Flexible Ethylene Sensor for Plant Stress Monitoring in Real-time

Nafize I. Hossain, Tanzila Noushin, and Shawana Tabassum, *Member, IEEE*

***Abstract*—This paper presents a flexible tattoo sensor for real-time monitoring of gaseous ethylene released from plant leaves. To the best of our knowledge, this is the first reported plant tattoo sensor that can measure and monitor a plant hormone *in situ*. The tattoo sensor can be easily installed on leaves and removed when required using a stick-and-peel mechanism. Furthermore, temperature and humidity sensors were incorporated to correct the ethylene measurements based on the specific microclimate of the leaf. All sensors were chemiresistive in nature, causing variations in resistance as a result of changes in temperature, humidity, or ethylene. The ethylene sensor demonstrated a sensitivity of 0.6295 kΩ/ppm and a limit of detection of 0.13 ppm. The measurements were processed by an onboard data logger, transmitted wirelessly to the cloud, and accessed on a smartphone. Plants were subjected to multiple stressors, including water, temperature, and dark stressors, and the real-time ethylene measurements were recorded with the tattoo sensor. A statistically significant difference, characterized by p values less than 0.05, was observed between different types of stresses. Roll-to-roll fabrication of these tattoos will enable their large-scale implementation in greenhouses and agricultural fields.**

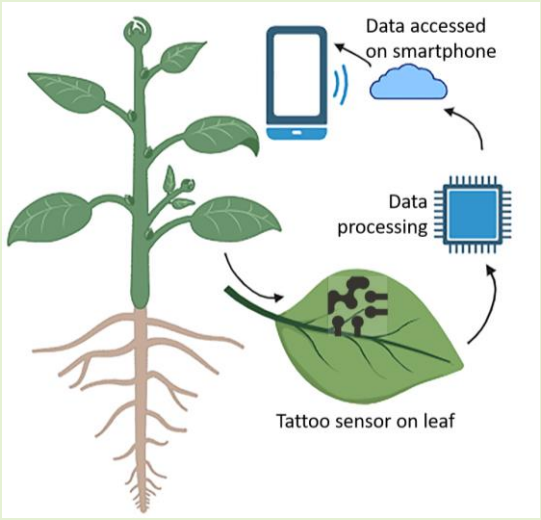

***Index Terms*—abiotic stress, electrochemical sensor, ethylene, plant hormone, plant wearables, tattoo sensor.**

I. Introduction

ETHYLENE is an important plant hormone that acts as a regulator for various physiological processes in plants, such as fruit ripening, flowering, leaf senescence [1]–[3], and responses to environmental stresses [4]–[6]. For example, ethylene biosynthesis is triggered by a variety of abiotic stress conditions, including heat, shade, low nutrient availability, and water deficiency [7]–[9]. Increased ethylene emissions in response to an external stressor lead to a decrease in the plant's growth rate, which helps regulate the resource allocation dynamics [10]. These altered dynamics decrease the demand for limited resources available during the period of stress. Hence, real-time detection of ethylene provides valuable insights into the internal dynamics of plants, enabling farmers, agronomy researchers and horticulturists to detect stress conditions early. Such real-time information on plant health aids in minimizing crop productivity losses and facilitates optimal timing for harvesting, storage, and transportation of crops. Although significant research attention has been given on investigating the role of ethylene in responses to abiotic stress conditions, there is a lack of low-cost and *in situ* detection technologies to measure the dynamics of ethylene emission from plants in real-time.

Currently, gas chromatography-mass spectrometry (GC-MS) is the primary gold-standard technique used to measure and analyze gases. Although GC-MS methods are highly sensitive and selective, they are limited to laboratory settings, are non-continuous, time-consuming, laborious, and expensive (>$100k) [11]. Recent studies report the availability of commercial portable gas flux chambers and gas analyzers that employ Fourier transform infrared (FTIR) spectroscopy (>$50k), cavity ring-down spectroscopy (>$85k), and infrared photoacoustic spectroscopy (>$50k) for on-site gas monitoring [12]. Although the spectroscopic techniques are highly sensitive, they are expensive and not an affordable solution for producers (as was also identified during our interviews with Texas farmers and precision farming companies such as BASF and Corteva, as part of the 2021 Southwest Innovation Corps site program). The current method of gas collection from whole plants requires large canopy chambers, which are not ideal for high-throughput monitoring of gas fluxes in field conditions [13]–[16]. Some *in situ* plant monitoring techniques include infrared and thermal imaging methods.

This work was supported in part by the VentureWell Grant 21716-20, in part by the National Science Foundation Award No. ECCS 2138701, and in part by the National Aeronautics and Space Administration Award No. 80NSSC23K0401.

S. Tabassum is with the Electrical and Computer Engineering Department, the University of Texas at Tyler, Tyler, TX 75799 USA (e-mail: stabassum@uttyler.edu). N. Hossain and T. Noushin were affiliated with the Electrical and Computer Engineering Department, the University of Texas at Tyler, Tyler, TX 75799 USA when this study was conducted. Currently, N. Hossain is affiliated with the Electrical and Computer Engineering Department, Tufts University, Medford, MA 02155 USA (nafize_ishtiaque.hossain@tufts.edu) and T. Noushin is affiliated with the Electrical and Computer Engineering Department, the University of Texas at Dallas, Richardson, TX 75080 USA (tanzila.noushin@utdallas.edu).

XXXX-XXXX © XXXX IEEE. Personal use is permitted, but republication/redistribution requires IEEE permission.
See http://www.ieee.org/publications_standards/publications/rights/index.html for more information.
Authorized licensed use limited to: Iowa State University Library. Downloaded on May 12,2024 at 22:25:05 UTC from IEEE Xplore. Restrictions apply.
© 2023 IEEE. Personal use is permitted, but republication/redistribution requires IEEE permission. See https://www.ieee.org/publications/rights/index.html for more information.

This article has been accepted for publication in IEEE Sensors Journal. This is the author's version which has not been fully edited and
content may change prior to final publication. Citation information: DOI 10.1109/JSEN.2023.3327547

However, these imaging techniques rely on indirect quantification, lack accuracy, and do not provide quantitative analysis of biomolecules [17]. Remote sensing techniques using unmanned aerial systems do not provide chemical profiles of the plants and are very power-hungry, frequently requiring human intervention for battery recharge/replacement [18], [19]. There are no commercial *in situ* plant sensors available to provide real-time and continuous monitoring of hormonal changes in response to abiotic or biotic stress conditions.

Frequent and regular monitoring of plant health is crucial for early detection of stress conditions, executing timely intervention measures (e.g., adjusting irrigation, applying fertilizers, or implementing pest control measures), and data-driven decision-making (e.g., data on plant health trends and responses to different treatments can guide farmers in making an informed decision about their cultivation practices). Recent developments in the literature demonstrate notable advancements in gas sensors that may allow continuous and real-time monitoring of ethylene. These sensors utilize innovative electrode designs combined with nanomaterials and their conjugates or metal oxides to enhance the sensor's performance in terms of sensitivity, selectivity, accuracy, response time, and real-time monitoring capabilities [20]. In this regard, electrochemical sensors have garnered much attention. Unlike the optical gas sensing systems that are expensive and lack portability due to the involvement of bulky light source and detectors [21], [22], miniaturized electrochemical sensors are more feasible for direct plant applications. Several electrochemistry-based ethylene sensors have been reported in the literature. Our previous work featured a three-electrode based ethylene sensor fabricated on a Nafion substrate [23]. Although the sensor demonstrated a high sensitivity to gaseous ethylene released from plant leaves, the three-electrode-based amperometric setup necessitated the use of a solid-state electrolyte, which Nafion serves as. As a result, the choice of substrate was limited, which hindered the integration of multiple sensors on the same substrate. Moreover, amperometric detection increased the complexity and footprint of the data logger. Likewise, other amperometric ethylene sensors relied on a solid polymer electrolyte [24] or an ionic liquid [25], requiring either specific substrate or fabrication technique as well as lacking flexibility and multiplexing capability on the same substrate. Another work reports a chemiresistive ethylene sensor on a glass slide [26]. The sensor employed a conjugate coating made from single-walled carbon nanotube and a copper cofactor that bound to sub-ppm levels of ethylene. However, owing to the formation of the electrodes on a rigid substrate, the sensor is not suitable for direct attachment to plants. Additional examples include activation chemistry-based ethylene detection [27]; however, a field-deployable sensor has not been materialized yet.

This study takes a stride toward the realization of a novel wearable leaf sensor for monitoring ethylene gas in real-time. The sensor features a tattoo-like framework that can be directly applied to plant leaves and easily removed when needed using a simple stick-and-peel mechanism. Additionally, the sensor is flexible and non-invasive, allowing continuous monitoring of plant health. The ethylene sensor comprises a two electrode-based chemiresistive surface coated with a conjugate of copper complex and single-walled carbon nanotubes, which enables reversible interactions with gaseous ethylene [26]. Moreover, temperature and humidity sensors are incorporated on the same tattoo substrate to investigate the role of leaf temperature and humidity on ethylene emission. Consequently, temperature and humidity corrections are applied to the ethylene measurements. The sensor demonstrates a high sensitivity of 0.6295 kΩ/ppm to ethylene with a limit of detection (LOD) of 0.13 ppm. The multiplexed tattoo sensor is also installed on the leaves to monitor ethylene gas emitted from the plants subjected to different combinations of water, heat, and dark stressors. Furthermore, statistical analyses are performed to establish a correlation between the ethylene levels released in response to varying combinations of stress factors. The results of this study will be extremely valuable to producers, enabling them to modify resource allocation and reduce crop productivity losses based on the real-time ethylene measurements.

II. Materials and Methods

Tetra chloroauric (III) acid ($HAuCl_4.H_2O$), sodium citrate, chitosan, ammonium hydroxide, polyvinylpolypyrrolidone (PVPP), hydroxyethyl cellulose (HEC), diethyl ether, [3,5-$(CF_3)_2$-pyrazol-1-yl], copper (I) trifluoromethane sulfonate benzene complex, sodium borohydride ($NaBH_4$), toluene, 1,2-dichlorobenzene, graphene ink in ethanol, and silver/silver chloride (Ag/AgCl) paste were purchased from Sigma Aldrich, St. Louis, MO, USA. Multi-walled carbon nanotubes (MWCNT) and single-walled carbon nanotubes (SWCNT) were procured from ACS Material, LLC, Pasadena, CA, while sulfuric acid and nitric acid were obtained from Thermo Fisher Scientific, Waltham, MA, USA. The tattoo paper (Model: MEDIA-TATTOO) was procured from Silhouette America.

A USCutter (Tukwila, WA, USA) programmable automated cutting machine (PrismCut, Model P20) was employed to manufacture the sensors. Computer-aided designs (CAD) were generated using AutoCAD Fusion 360 software by Autodesk Inc., San Rafael, CA, USA. The Applent AT 3817 LCR meter was utilized to determine the resistance for calibrating the sensors. To visualize the structure and morphology of coated surfaces, a JSM-IT800SHL Scanning Electron Microscope (SEM) was utilized. For the identification of functional groups and characterization of covalent bonding within the coatings, a Nicolet Avatar 360 E.S.P ATR-FTIR (Attenuated Total Reflectance-Fourier Transform Infrared) spectrometer was employed. The stress-strain behavior of the device was evaluated using a motorized translation stage (MTS50-Z8) and a brushed DC servo motor controller (KMTS5E) from Thorlabs Inc., based in Newton, NJ, USA. During the calibration and selectivity assessments of the ethylene sensor, a mass flow controller (MFC) (EW-32658-06) from Cole-Parmer in Vernon Hills, IL, USA, was used to control gas flow.

III. Sensor Fabrication and System Integration

Fabrication of the sensors commenced with the printing of electrodes onto a flexible tattoo-like framework followed by functionalization of sensitive materials on the electrode surfaces. Subsequently, the sensing structure was interfaced with an Internet-of-Things (IoT)-enabled data logger for data

Authorized licensed use limited to: Iowa State University Library. Downloaded on May 12,2024 at 22:25:05 UTC from IEEE Xplore. Restrictions apply.
© 2023 IEEE. Personal use is permitted, but republication/redistribution requires IEEE permission. See https://www.ieee.org/publications/rights/index.html for more information.

This article has been accepted for publication in IEEE Sensors Journal. This is the author's version which has not been fully edited and
content may change prior to final publication. Citation information: DOI 10.1109/JSEN.2023.3327547

acquisition, processing and transmission. The process flow for sensor fabrication and system integration is outlined below.

A. Fabrication of Multiplexed Electrodes on a Tattoo Substrate

The tattoo paper was procured from Silhouette America. Fabrication of the tattoo-like electrodes began by placing a paper substrate, covered with adhesive-backed transfer tape, onto the programmable cutter (Fig. 1a-b). Subsequently, the CAD design of electrodes was loaded to the PrismCut cutter. The cutter carved out electrode designs for ethylene, temperature, and humidity sensors on the same transfer tape (Fig. 1c-d) utilizing a blade with a 30° slanted tip, operating at an optimized speed of 30 mm/s and a force of 4 N. Subsequent stages involved the application of conductive inks through screen printing. Firstly, the transfer tape was peeled off from the sections designated for the electrodes. A squeegee was utilized to evenly apply a layer of graphene paste onto the sheet, as illustrated in Fig. 1e. The sheet was heated in the oven at 100°C for 45 minutes. Finally, the transfer tape was removed from the remaining sections, resulting in the transfer of the electrodes to the underlying paper sheet. Fig. 1f displays the electrodes for ethylene (ET), temperature (T) and relative humidity (RH) sensors. The entire paper sheet measured 10 mm x 10 mm. The active circular regions of the ET and RH sensors had a diameter of 2 mm. Different dimensions of the T sensor are shown in Fig. 1f. Afterwards, a sticker sheet (having a blue paper backing) was attached to the back side of the paper sheet, as depicted in Fig. 1g-h. The combined sheet was then placed on the back side of the leaf (Fig. 1i), and the blue paper backing was removed. Following this step, a damp cloth was applied to press the remaining paper substrate containing the electrodes for about 10 minutes (Fig. 1j). This process facilitated the detachment and removal of the paper sheet, leading to the transfer of electrodes onto the sticker, creating a tattoo-like device (Fig. 1k). Fig. 1l illustrates a visual representation of the tattoo sensor installed onto the leaf of a bell pepper plant.

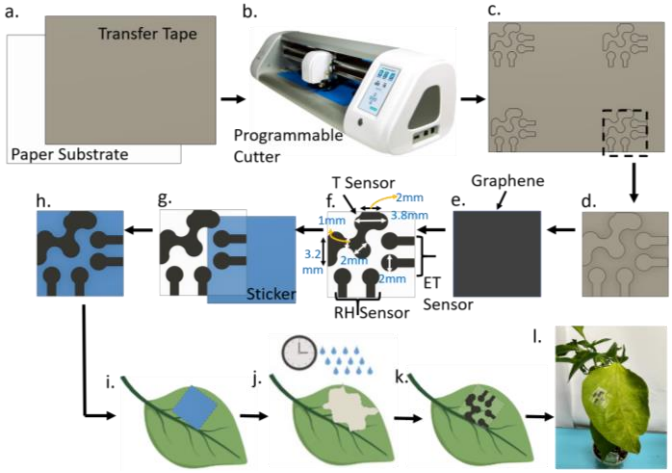

Fig. 1. Fabrication steps of the tattoo sensor: (a) A paper-backed transfer tape is loaded to the (b) programmable cutter. (c) An array of electrode patterns is carved on the combined sheet. (d) A single piece of electrode design is cut out from the array. (e) Transfer tape from the electrode areas is removed and subsequently graphene is screen-printed on the entire sheet. (f) The transfer tape is removed from the remaining areas of the sheet, resulting in electrodes transferred to the paper substrate. (g) – (h) A sticker sheet is attached to the back side of the paper sheet. (i) The sticker is attached to the leaf. (j) The blue paper backing is removed from the sticker and a moist cloth is pressed onto the electrodes to remove the residual paper. (k) The electrodes are transferred onto the leaf and stay in place like a tattoo. (l) Optical image of the tattoo sensor placed on the leaf of a bell pepper plant.

B. Functionalization of Temperature and Humidity Sensors

The electrode of the temperature sensor was modified by incorporating multiwalled carbon nanotubes (MWCNTs) mesh embedded with gold nanoparticles (AuNPs). We employed the Au-MWCNT composite in this study owing to the adjustable electrical conductivity, improved mechanical characteristics, and strong interfacial bonding of MWCNT with the underlying polymer (in this case the sticker substrate) enabling high stretchability/bendability [28]–[31] and the enhanced electrical conductivity contributed by Au nanoparticles [32]. The procedures for synthesizing the AuNP-MWCNT composite are outlined below. Initially, a 0.01% (w/v) solution of tetra chloroauric (III) acid ($HAuCl_4.H_2O$) was reduced by 1% (w/v) sodium citrate using the Turkevich method to generate AuNPs [33]. Simultaneously, a 1% (w/v) solution of MWCNT was dissolved in chitosan and sonicated for 8 hours, producing the MWCNT suspension solution. Subsequently, equal volumes of the MWCNT dispersion and AuNP solution were mixed and sonicated for 2 hours to form a 1% (w/v) AuNP-MWCNT conjugate. The solution was allowed to settle for a day to facilitate the integration of AuNPs into the MWCNT network. Finally, 300 µL of the AuNP-MWCNT solution was deposited onto the graphene electrode, followed by air drying at room temperature for 3 hours.

The specialized coating for the humidity sensor consisted of hydroxyethyl cellulose (HEC) and functionalized multiwalled carbon nanotube (f-MWCNT). The MWCNT underwent modifications to enhance its hydrophilicity and to achieve a uniform dispersion within an aqueous solution [34], [35]. The modification process involved introducing hydroxyl (-OH) groups to the MWCNT through acid treatment. Initially, 125 mg of MWCNT was combined with a mixture of sulfuric acid and nitric acid in a 3:1 (v/v%) ratio. The resulting mixture was stirred at 800 rpm for 3.5 hours while maintaining a reflux temperature of 140°C. After the reflux and stirring were halted, the mixture was cooled to room temperature. Ammonium hydroxide was then added to adjust the solution's pH to 5.5. The f-MWCNT was subsequently filtered using a 0.2 µm polytetrafluoroethylene (PTFE) membrane under vacuum and then subjected to 150°C convection oven heating for 12 hours. Following this step, a 1.25 wt% dispersion of f-MWCNT in deionized (DI) water was prepared. Continuous magnetic stirring was employed for 3 hours to prevent DI water evaporation. Subsequently, mixtures of f-MWCNT and HEC were prepared using four different weight ratios (1:4, 1:2, 1:1, and 2:1) and stirred for 3 hours. Notably, HEC, due to its hygroscopic nature, exhibited high solubility in water, preventing f-MWCNT from aggregating [36]. The mixture of f-MWCNT and HEC underwent 72 hours of continuous stirring to yield a homogeneous solution. Next, a solution containing 50 wt% polyvinylpolypyrrolidone (PVPP) was introduced with a binder-to-filler ratio of 1:2, and the resulting mixture was stirred for 8 hours to ensure uniformity. This ink

Authorized licensed use limited to: Iowa State University Library. Downloaded on May 12,2024 at 22:25:05 UTC from IEEE Xplore. Restrictions apply.
© 2023 IEEE. Personal use is permitted, but republication/redistribution requires IEEE permission. See https://www.ieee.org/publications/rights/index.html for more information.

This article has been accepted for publication in IEEE Sensors Journal. This is the author's version which has not been fully edited and
content may change prior to final publication. Citation information: DOI 10.1109/JSEN.2023.3327547

was evenly applied onto the humidity sensing electrodes to form the humidity sensor. The optimal f-MWCNT to HEC weight ratio of 1:4, with f-MWCNT having a length of 10nm, exhibited the highest sensitivity to changes in humidity levels. As a result, all subsequent measurements were conducted using a f-MWCNT to HEC weight ratio of 1:4.

C. Functionalization of Ethylene Sensor

The procedure outlined in our previous research [21], [23] was followed to create the copper complex (I) solution. Initially, a combination of 0.4g of $NaBH_4$ and 7.55g of [3,5-$(CF_3)_2$-pyrazol-1-yl], also referred to as 3,5-$(CF_3)_2$-pz, was mixed with kerosene in a conical vessel to form a uniform mixture. This mixture was gradually heated to 190°C with a heating rate of 1°C per minute and maintained at that temperature for a duration of 4 hours. Throughout the heating process, the vessel was partially immersed in silicone oil. To facilitate the melting of pyrazole, the solution was periodically heated using a heat gun every 15 minutes. Afterward, the solution was cooled to room temperature, and diethyl ether was introduced to remove excess reagents. The resulting white solid was subjected to nuclear magnetic resonance (NMR) analysis to validate the formation of the product, Na[HB(3,5-$(CF_3)_2$-pz)$_3$]. Subsequently, 8mg of copper(I) trifluoromethane sulfonate benzene complex was dissolved in 3 mL dry, degassed toluene. Then, 17 mg of Na[HB(3,5-(CF3)2-pz)3] was added, and the mixture was stirred for 20 hours at room temperature. A Whatman 0.02 µm syringe filter was used to filter the solution, resulting in a colorless solution of copper complex-1.

In a separate container, 0.5 mg of SWCNT was combined with a mixture of 0.8 mL 1,2-dichlorobenzene and 1.16 mL toluene. This mixture was sonicated for 2 hours to achieve a uniform solution. Subsequently, the freshly prepared copper complex-1 solution was added, and another round of sonication was performed for 1 hour. Finally, a volume of 30 µL of this solution was drop-cast between the two electrodes, ensuring complete coverage of both electrode surfaces.

D. IoT-enabled Data Logger

Each of the temperature, humidity, and ethylene sensors were resistive by nature. The conductance/resistance of the functionalized coating altered in response to changes in temperature, relative humidity, or ethylene gas. In order to render the system wearable and collect real-time measurements from plants, an onboard data logger was built. Each sensor was connected in a series configuration with a predetermined resistor, creating a voltage divider circuit. A consistent 3.3 V voltage was applied across the voltage divider and the alterations in resistance observed in the sensors were transformed into voltage readings. The primary central processing unit of the data logger was an ESP32 microcontroller featuring integrated WiFi capabilities. The ESP32 microcontroller was equipped with a built-in analog-to-digital converter (ADC) that gauged the voltage across each sensor, translating the analog voltages into digital values. The voltage measurement, denoted as V, was determined using the ADC readings through the formula V = (ADC Reading * DC input voltage) / (2^n - 1), where the DC input voltage was 3.3V and n = 8. The ESP32 microcontroller processed data

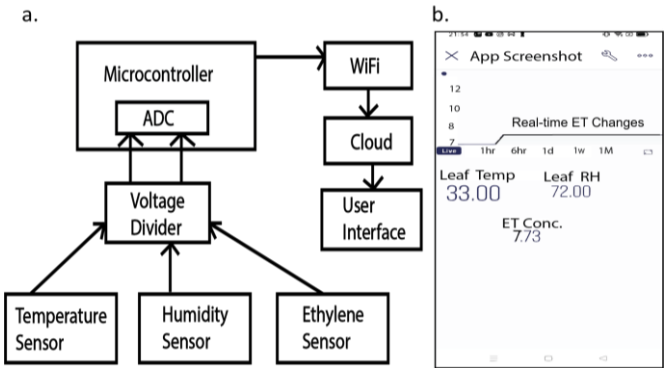

Fig. 2. (a) Block diagram of the system where the sensors are interfaced with the data logger. (b) Screenshot of the Blynk application that shows leaf temperature (T), relative humidity (RH) and ethylene (ET) levels in real-time.

from the sensors to derive unknown values of temperature, relative humidity, and ethylene concentration by referencing pre-established calibration plots. Ultimately, temperature, humidity, and ethylene measurements were transmitted to the cloud, as shown schematically in Fig. 2a. These measurements were conveniently accessed through a smartphone application utilizing the Blynk IoT interface, as depicted in Fig. 2b.

IV. Characterization Tests

All the three sensors underwent microscopic and spectroscopic characterizations in order to analyze the morphology and chemical bonds of the functionalized coatings. Subsequently, the sensors were evaluated for sensitivity, selectivity, bendability, and repeatability. The results are discussed below.

A. Microscopic and Spectroscopic Analysis

Fig. 3a displays the scanning electron microscopy (SEM) depiction of the MWCNT coating adorned with AuNPs. This SEM image elucidates the arrangement and structure of the intertwined conductive MWCNT network, with an average CNT diameter of 20 nm. Fourier Transform Infrared (FTIR) spectroscopy (Fig. 3b) was employed for the characterization of the chemical bonds present in the MWCNT coating. The absorption bands between 3500 cm^{-1} and 4000 cm^{-1} were attributed to -OH functional groups. Peaks in the 1100-1160 cm^{-1}, 1390-1700 cm^{-1}, and 2975-3065 cm^{-1} ranges verified the presence of C-H bonds. The C-O bonds are represented by the peaks centered at 1600 and 1790 cm^{-1}. The wider peaks between 1950 and 2210 cm^{-1} were influenced by the characteristics of the diamond ATR (Attenuated Total Reflectance) setup. This FTIR spectrum corresponds with findings from earlier studies [32], [37].

The dimensions, arrangement, and structure of the copper complex (I) nanoparticles on the ethylene sensing electrode were revealed by the SEM imagery (Fig. 3c). These nanoparticles displayed an average diameter of approximately 10 nm. Additionally, a pivotal stage during the synthesis of the copper complex (I) coating involved precise creation of the intermediate substance Na[HB(3,5-$(CF_3)_2$-pz)$_3$]. To confirm the formation of this intermediary product, nuclear magnetic resonance (NMR) spectroscopy was employed, as illustrated in Fig. 3d. The spectroscopic findings provided validation for the presence of the Na[HB(3,5-$(CF_3)_2$-pz)$_3$] product.

Authorized licensed use limited to: Iowa State University Library. Downloaded on May 12,2024 at 22:25:05 UTC from IEEE Xplore. Restrictions apply.
© 2023 IEEE. Personal use is permitted, but republication/redistribution requires IEEE permission. See https://www.ieee.org/publications/rights/index.html for more information.

This article has been accepted for publication in IEEE Sensors Journal. This is the author's version which has not been fully edited and
content may change prior to final publication. Citation information: DOI 10.1109/JSEN.2023.3327547

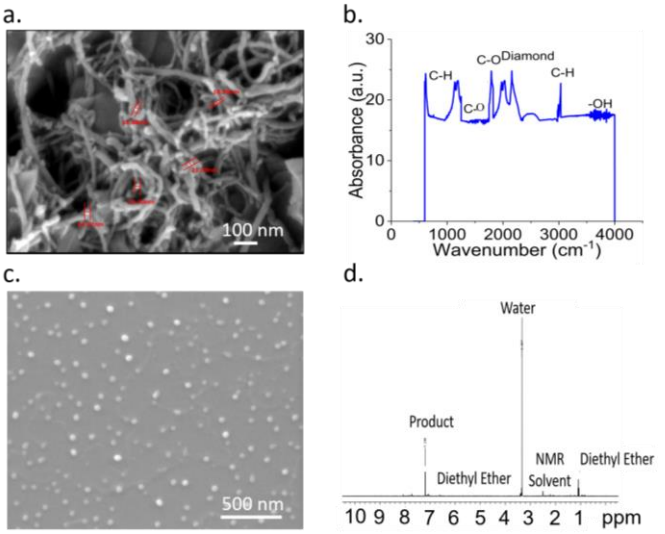

Fig. 3. (a) A higher magnification scanning electron microscopy (SEM) image illustrating the MWCNT fiber network, with the fiber diameter ranging from 11 to 25 nm (illustrated by the overlaid red lines and texts). (b) Fourier Transform Infrared (FTIR) spectroscopy analysis of MWCNT. (c) SEM depiction of copper complex (I) nanoparticles on the ethylene sensing electrode. (d) NMR analysis of the Na[3,5-$(CF_3)_2$-pz] ether blend to confirm the formation of the Na[3,5-$(CF_3)_2$-pz] product.

B. Performance Evaluation of Temperature and Humidity Sensors

The temperature sensor was calibrated by applying temperature values ranging from 25°C to 70°C. The resistance of AuNP-MWCNT conjugate, due to its negative temperature coefficient, decreased as temperature increased [30]. The resulting calibration curve for the temperature sensor exhibited strong linearity, characterized by a Pearson correlation coefficient of 0.98 (depicted in Fig. 4a). Furthermore, the temperature sensor was subjected to different relative humidity (RH) values spanning from 20% to 90%, as illustrated in Fig. 4a. Across this RH range, the sensor's response displayed a marginal fluctuation of 8.56%, indicating its suitability for field applications. The selection of temperature and RH values was based on their common occurrence within agricultural fields in the southern U.S. The calibration curve of the temperature sensor was repeated when the flexible tattoo substrate underwent bending at a 40° angle for 50 and 100 cycles, as is illustrated in Fig. 4b. Even following 100 bending cycles, the coefficient of variance among the calibration curves remained consistently below 9%. The temperature sensor also exhibited repeatable behavior during cyclic variations in temperature (depicted in Fig. 4c), with a coefficient of variance lower than 1%, which is deemed acceptable for operational reliability in field settings.

Likewise, the humidity sensor was calibrated for RH values ranging from 10% to 90%. An increase in the resistance value was observed with increasing RH values, as shown in Fig. 4d. The resistance versus relative humidity measurements were fitted with a power series equation, yielding an r-squared value of 0.98. The humidity sensor was exposed to varying levels of temperature, ranging from 20ºC to 50ºC, as depicted in Fig. 4d. Throughout this range of RH, the sensor's output exhibited a coefficient of variance of about 2.33%. Subsequently, the bending (Fig. 4e) and repeatability (Fig. 4f) tests exhibited coefficients of variance less than 10% and 0.5%, respectively.

The sensitivity and detection limit of the sensors are tabulated in Table I. The method outlined in [38] was used for sensitivity calculations of the nonlinear RH sensor.

TABLE I
KEY PERFORMANCE METRICS OF THE SENSORS

Sensor	Calibration Equation	Sensitivity	Detection Limit
Temperature (T)	R = -0.0278T +2.4262	-0.0278kΩ/°C	19.25°C
Relative Humidity (RH)	R = $0.004(RH)^{2.18}$ +1.38	0.1319kΩ/% at 10% RH 1.7641 kΩ/% at 90% RH	11.11 %
Ethylene (ET)	R = 0.6295*(ET conc) + 0.72806	0.6295 kΩ/ppm	0.13 ppm

C. Performance Evaluation of Ethylene Sensor

The ethylene sensor was calibrated by exposing it to different concentrations of gaseous ethylene, including 0.1 ppm, 1 ppm, 10 ppm, 30 ppm, 50 ppm, 75 ppm, and 115 ppm. Upon encountering ethylene, the copper complex (I) interacted with ethylene to create a secondary complex, which limited doping of the single-walled carbon nanotubes by the copper complex (I). Consequently, the conductivity of the single-walled carbon nanotubes declined, leading to an increase in the resistance measured across the two electrodes. The resistance versus concentration plot illustrated in Fig. 4g demonstrates the linear increase in the resistance with increasing concentrations of ethylene. Table I outlines the sensitivity and detection limit of the ethylene sensor. During this experiment, the sensor was placed inside a closed chamber where different concentrations of ethylene were introduced. The dimensions of the sensing chamber were 30.48 cm x 30.48 cm x 20.32 cm, resulting in a volume of 18877.8977 cm^3. At first, the chamber was purged with dry nitrogen to eliminate any moisture. Prior to entering the chamber, the ethylene gas was pre-diluted with nitrogen. A mass flow controller (MFC) (model EW-32658-06, Cole-Parmer, Vernon Hills, IL, USA) was used to regulate the flow rate of ethylene and nitrogen gases. While maintaining a constant flow rate of dry nitrogen at 10 cm^3/s within the chamber, the flow rate of ethylene was adjusted using the MFC to achieve different concentrations.

Considering the changes in temperature and humidity levels experienced in an agricultural field, we assessed the performance of the ethylene sensor in response to varying temperature and humidity conditions. The calibration plots for the ethylene sensor under different temperature and humidity levels are presented in Fig. 4h and Fig. 4i, respectively. Notably, the coefficient of variance across these calibration plots was determined to be below 5%. Yet, temperature and humidity corrections were applied to the ethylene concentration dynamics, using the Equations (1) – (6) provided below [39]. This is based on the assumption that the impacts of temperature and humidity on the ethylene sensor

Authorized licensed use limited to: Iowa State University Library. Downloaded on May 12,2024 at 22:25:05 UTC from IEEE Xplore. Restrictions apply.
© 2023 IEEE. Personal use is permitted, but republication/redistribution requires IEEE permission. See https://www.ieee.org/publications/rights/index.html for more information.

This article has been accepted for publication in IEEE Sensors Journal. This is the author's version which has not been fully edited and content may change prior to final publication. Citation information: DOI 10.1109/JSEN.2023.3327547

(specifically, the conjugate coating of copper complex and single walled carbon nanotubes) are distinct from one another, and that each ethylene sensor is uniformly affected by variations in temperature and humidity. Toward this end, the correction factors for the y-intercept and slope of the calibration curve were computed for various temperature and humidity conditions, compared to the reference conditions of 25°C temperature and 60% relative humidity, utilizing Equations (1) – (4). Subsequently, the corrected values of y-intercept and slope were determined utilizing the Equations (5) – (6). These corrected y-intercept and slope along with the measured resistance values were used to calculate the corrected ethylene concentration.

$$f_{intercept(temp)} = \frac{\text{int}\,ercept_{temp}}{\text{int}\,ercept_{25\circ C}} \quad \text{.....(1)}$$

$$f_{intercept(\%RH)} = \frac{\text{int}\,ercept_{\%RH}}{\text{int}\,ercept_{\%60}} \quad \text{.....(2)}$$

$$f_{slope(temp)} = \frac{slope_{temp}}{slope_{25\circ C}} \quad \text{.....(3)}$$

$$f_{slope(\%RH)} = \frac{slope_{\%RH}}{slope_{\%60}} \quad \text{.....(4)}$$

$$\text{int}\,ercept_{corr.} = \text{int}\,ercept_{init.} \times f_{intercept(temp)} \times f_{intercept(\%RH)} \quad \text{..(5)}$$

$$slope_{corr.} = slope_{init.} \times f_{slope(temp)} \times f_{slope(\%RH)} \quad \text{.....(6)}$$

The performance of the ethylene sensor was evaluated in presence of different interfering gases and their mixtures, including: (i) 50 ppm of nitrogen (N_2), (ii) 50 ppm of methane (CH_4), (iii) 50 ppm of nitrous oxide (N_2O), (iv) 50 ppm of ammonia (NH_3), (v) a mixture of 50 ppm of N_2, CH_4, N_2O, NH_3, each, (vi) a mixture of 50 ppm of N_2, CH_4, N_2O, NH_3, each and 1 ppm of ethylene, (vii) 1 ppm of ethylene, (viii) a mixture of 50 ppm of N_2, CH_4, N_2O, NH_3, each and 10 ppm of ethylene, and (ix) 10 ppm of ethylene. The measured resistance values were significantly less for the interfering gases compared to when ethylene was present in the mixture (Fig. 4j). These results indicate that the sensor demonstrated a much higher selectivity towards ethylene than other gases.

Similar to the temperature and humidity sensors, the ethylene sensor was subjected to repeated bending deformations upto 60 and 100 cycles at 40º bending angle. The resulting calibration plots in Fig. 4k show a coefficient of variation of about 2.311%. Furthermore, upon cyclic exposure to ethylene concentrations, the sensor exhibited a negligible coefficient of variance of less than 0.5% (Fig. 4l). These results confirm the reversible binding between copper complex and ethylene.

D. Evaluation of Failure Point, Stability, and Accuracy

To investigate the failure point of the sensors, we conducted repeated bending tests at 50° and 60° bending angles, as shown in Fig. 5. These tests revealed that the ethylene, temperature, and humidity sensors exhibited variations of up to 28%, 200%, and 200%, respectively, in their responses when bent at a 50° angle. Moreover, the sensors failed to withstand more than 30 cycles of bending at a 60° angle, which we consider as the failure point of the sensors.

The settling time and percentage overshoot of ethylene (ET), temperature (T), and humidity (RH) sensors are:
(i) Settling time (defined as the time for the response to reach and stay within 2% of its final value):
ET = 0.088s, T = 0.215s, RH = 0.231s

(ii) Percentage overshoot:
ET = 6.80%, T = 16.14%, RH = 15.97%

.

The percentage overshoot (%OS) is calculated using the following formula [40], with C_{max} and C_{final} representing the maximum and final values, respectively:

$$\%OS = \frac{c_{\max} - c_{final}}{c_{final}} \times 100 \quad \text{.....(7)}$$

Fig. 6a-c graphically represent the time required by the ethylene, temperature, and humidity sensors to settle down.

Furthermore, we analyzed the long-term stability of the sensors over 30 days, as shown in Fig. 6d-f. It was noted that the ethylene and humidity sensors exhibited a consistent response until Day 12, after which the response gradually decreased. In contrast, the temperature sensor was very stable over the entire 30-days period.

The approach used to validate the reliability of our ethylene sensor is explained in our prior work [23]. Briefly, we adopted an indirect approach to analyze the ethylene gas directly emitted from plant leaves. First, we calibrated our ethylene sensor for a known set of ethylene concentrations mixed with other interfering gases (i.e., N_2, CH_4, N_2O, and NH_3). Next, the sensor responses were recorded for unknown ethylene concentrations emitted from the plant. Afterward, the sensor was exposed to a range of known ethylene concentrations to find out the concentrations at which the sensor response approximately matched with the responses recorded for unknown ethylene emitted from plants. The results are plotted in Fig. 7a, which show that our ethylene sensor has a very high accuracy, with a Pearson correlation coefficient of 0.98. Moreover, the temperature and humidity values measured with our sensors were compared against the values measured with commercially available temperature (LM35, Texas Instruments, TX) and humidity (DHT11, Adafruit, NY) sensors. The results are plotted in Fig. 7b-c, which show that our temperature and humidity sensors exhibit a high accuracy, with a Pearson correlation coefficient of more than 0.99.

V. On-Plant Evaluation

For conducting real-time plant measurements, the tattoo sensors were adhered to the back side of the leaves of bell pepper plants. This was done because stomata are small openings or pores that are typically present on the rear surfaces of leaves. These stomata open and close to regulate gas exchange and water loss [41], [42], making the back side of the leaf ideal for ethylene detection.

Authorized licensed use limited to: Iowa State University Library. Downloaded on May 12,2024 at 22:25:05 UTC from IEEE Xplore. Restrictions apply.
© 2023 IEEE. Personal use is permitted, but republication/redistribution requires IEEE permission. See https://www.ieee.org/publications/rights/index.html for more information.

This article has been accepted for publication in IEEE Sensors Journal. This is the author's version which has not been fully edited and
content may change prior to final publication. Citation information: DOI 10.1109/JSEN.2023.3327547

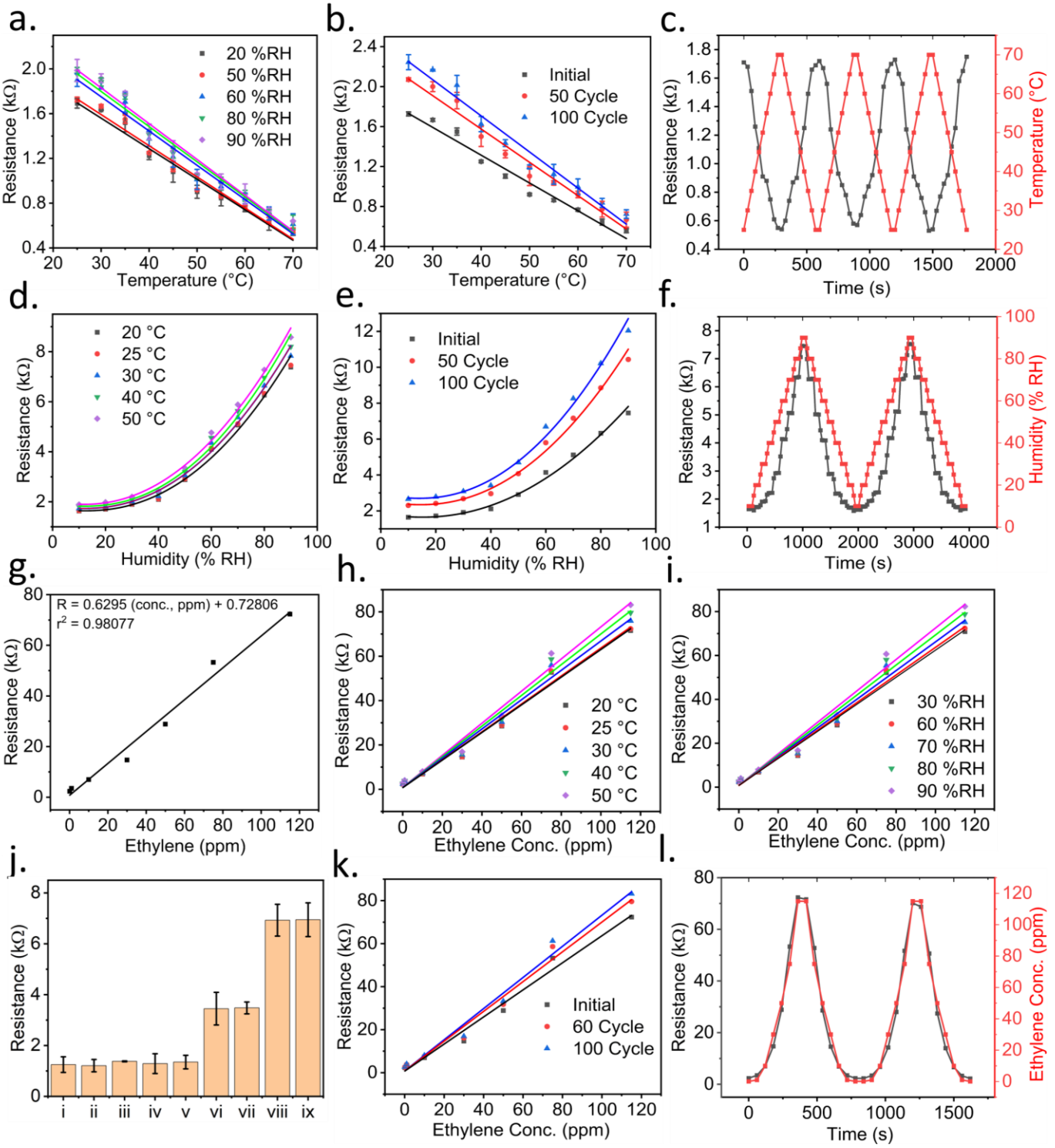

Fig. 4. (a) Calibration plots of the temperature sensor under varying relative humidity (RH) conditions. (b) Calibration plots of the temperature sensor under varying bending cycles. (c) Repeatability test for the temperature sensor. (d) Calibration plots of the humidity sensor under varying temperature conditions. (e) Calibration plots of the humidity sensor under varying bending cycles. (f) Repeatability test for the humidity sensor. (g) Calibration plot of the ethylene sensor at room temperature and 60% RH. (h) Calibration plots of the ethylene sensor under varying temperature conditions. (i) Calibration plots of the ethylene sensor under varying relative humidity (RH) conditions. (j) Selectivity test that shows resistance measurements of the ethylene sensor where i-ix represent: (i) 50 ppm of nitrogen (N_2), (ii) 50 ppm of methane (CH_4), (iii) 50 ppm of nitrous oxide (N_2O), (iv) 50 ppm of ammonia (NH_3), (v) a mixture of 50 ppm of N_2, CH_4, N_2O, NH_3, each, (vi) a mixture of 50 ppm of N_2, CH_4, N_2O, NH_3, each, and 1 ppm of ethylene, (vii) 1 ppm of ethylene, (viii) a mixture of 50 ppm of N_2, CH_4, N_2O, NH_3, each, and 10 ppm of ethylene, and (ix) 10 ppm of ethylene. (k) Calibration plots of the ethylene sensor under varying bending cycles at 40º angle. (l) Repeatability test for the ethylene sensor. Error bars in all the plots represent mean and standard error computed from three repeated measurements.

Authorized licensed use limited to: Iowa State University Library. Downloaded on May 12,2024 at 22:25:05 UTC from IEEE Xplore. Restrictions apply.
© 2023 IEEE. Personal use is permitted, but republication/redistribution requires IEEE permission. See https://www.ieee.org/publications/rights/index.html for more information.

This article has been accepted for publication in IEEE Sensors Journal. This is the author's version which has not been fully edited and
content may change prior to final publication. Citation information: DOI 10.1109/JSEN.2023.3327547

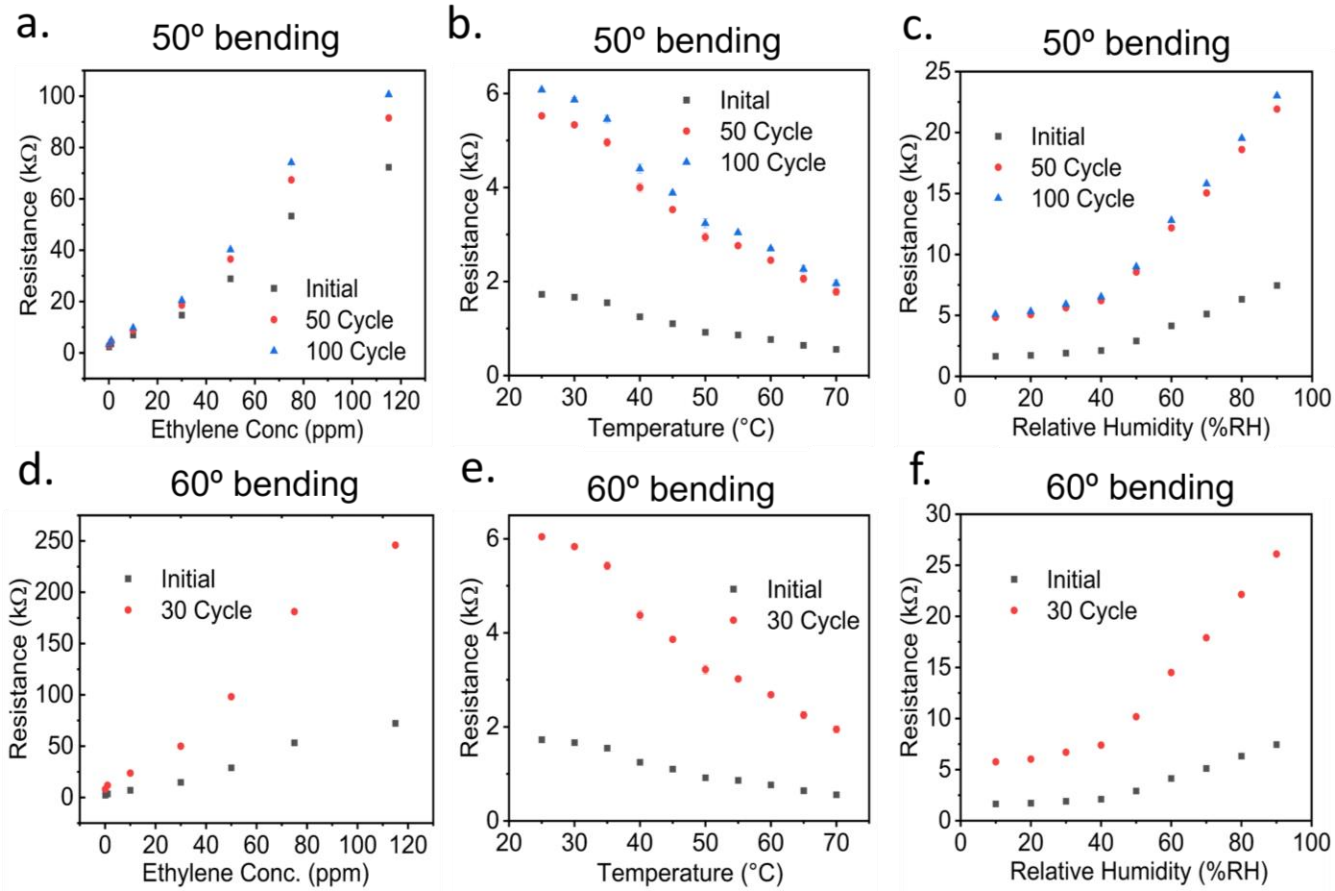

Fig. 5. Calibration plots of the (a) ethylene, (b) temperature, and (c) humidity sensors under 50 and 100 cycles of bending at 50º angle. Calibration plots of the (d) ethylene, (e) temperature, and (f) humidity sensors under 30 cycles of bending at 60º angle.

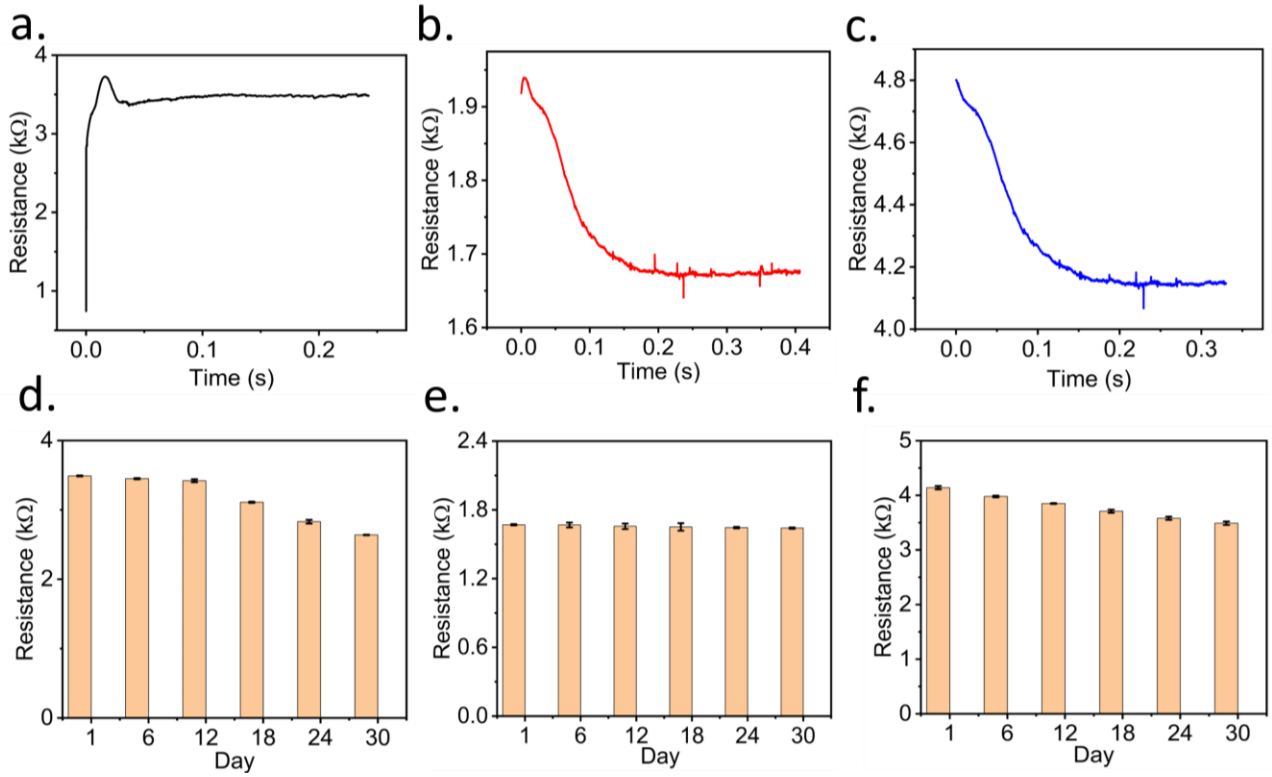

Fig. 6. Representation of settling time and overshoot: (a) Ethylene sensor response at 1 ppm, (b) Temperature sensor response at 30°C, (c) Humidity sensor response at 60%RH. Long-term stability over 30 days: (d) Ethylene sensor response at 1 ppm, (e) Temperature sensor response at 30°C, (f) Humidity sensor response at 60%RH.

Authorized licensed use limited to: Iowa State University Library. Downloaded on May 12,2024 at 22:25:05 UTC from IEEE Xplore. Restrictions apply.
© 2023 IEEE. Personal use is permitted, but republication/redistribution requires IEEE permission. See https://www.ieee.org/publications/rights/index.html for more information.

This article has been accepted for publication in IEEE Sensors Journal. This is the author's version which has not been fully edited and
content may change prior to final publication. Citation information: DOI 10.1109/JSEN.2023.3327547

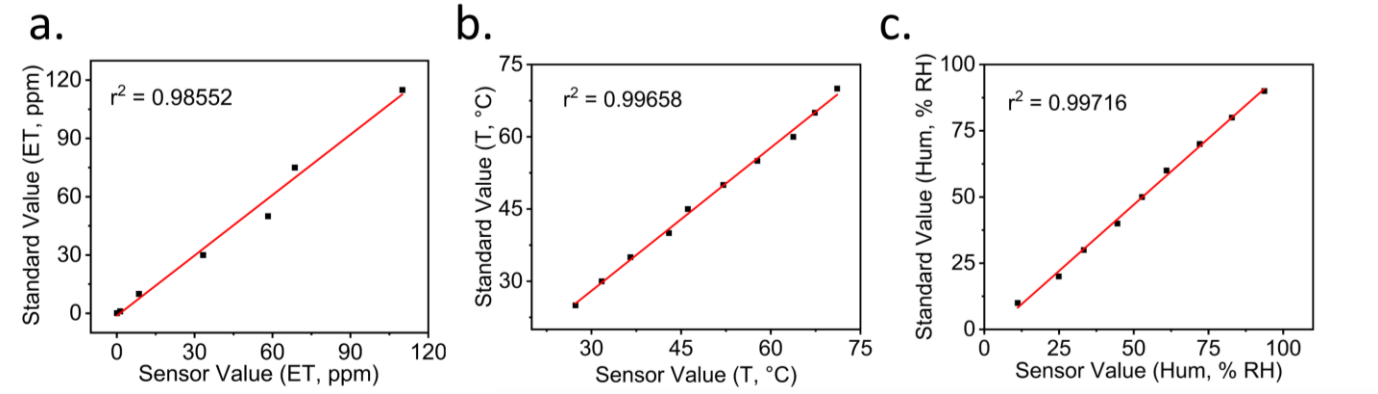

Fig. 7. Accuracy of (a) ethylene, (b) temperature, and (c) humidity sensors compared to standard measurement methods.

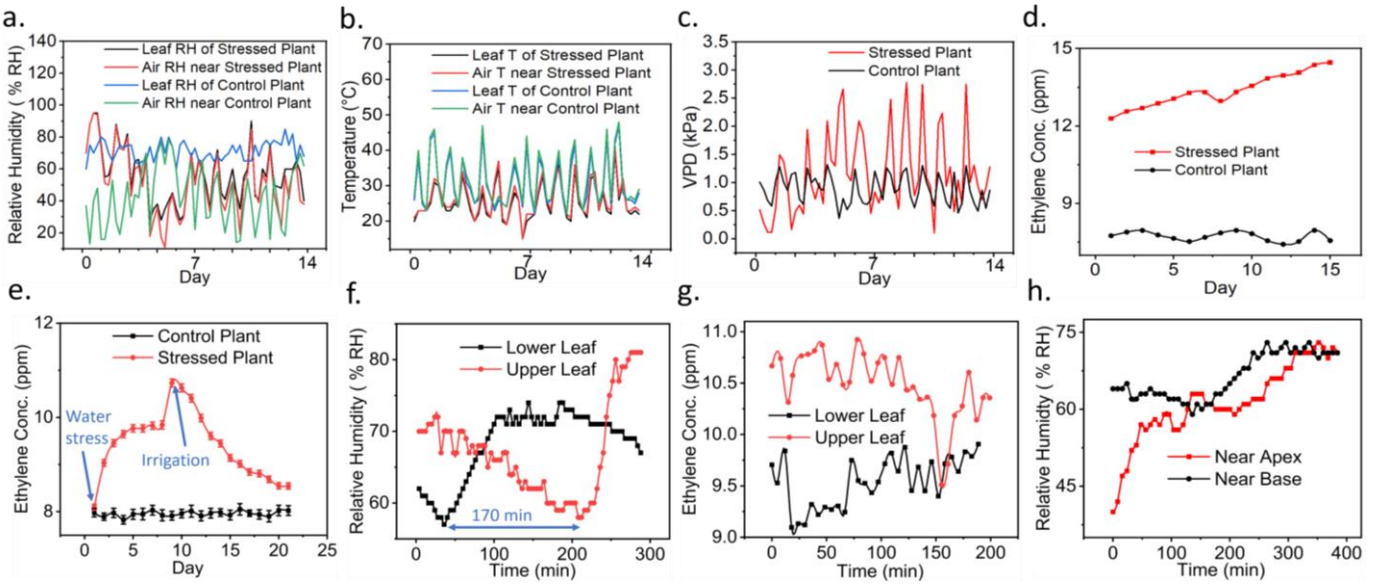

Fig. 8. (a) Relative humidity, (b) temperature, (c) VPD and (d) ethylene levels measured from control and stressed plants over 14 days. (e) Ethylene measurements under alternating cycles of water deficiency and irrigation. Measurements were repeated with 10 control and 10 stressed bell pepper plants, with error bars representing the standard error of plant-to-plant variations. (f) Dynamic relative humidity values measured at lower and upper leaves. (g) Dynamic ethylene concentrations measured at lower and upper leaves. The lower and upper leaves were located at 40 cm and 105 cm, respectively, above the soil surface. (h) RH dynamics measured at two locations of the same leaf located at 75 cm above soil.

A. Monitoring Ethylene Emission in Water Stressed Plants

A series of experiments were conducted with live bell pepper plants. The tattoo sensors were installed on the back side of the leaves. Ten plants were used as control plants, while another ten were subjected to water stress. No water was applied to the stressed plants throughout the stress period, while the control plants received a daily dose of 250 mL of water. Temperature, relative humidity, and ethylene measurements were recorded once a day. Fig. 8a-d illustrate the averages of measurements from 10 control and 10 stressed plants over 14 days. Several observations are evident from these results. Firstly, the relative humidity of air remained lower than the relative humidity levels recorded beneath the leaf (Fig. 8a). Furthermore, the temperature of the leaves (in both stressed and control plants) consistently stayed lower than the air temperature (Fig. 8b). These results attribute to the cooling effect caused by transpiration. The vapor pressure deficit (VPD) (calculated using the methodology outlined in [23]) was always higher in stressed plants as compared to the control plants (Fig. 8c). A similar trend was observed in ethylene measurements, as depicted in Fig. 8d. Stressed plants consistently emitted elevated levels of ethylene.

Next, the stressed plants underwent alternating cycles of water deficiency and irrigation schedule. As shown in Fig. 8e, the control plants consistently released a mean ethylene concentration of 7.95 ppm, with a standard deviation of 0.5 ppm. A temporal correlation was observed in the time-series data between the ethylene concentrations and the water stress periods. Ethylene levels exhibited a rise during water stress, and following irrigation on Day 9, there was an immediate decline in the ethylene levels. These results also offer insight into the implications of prolonged sensor attachment on plant performance. The results from our experiments showed that throughout the 21-day testing period, there was no notable stress induced by sensor attachment on the plants. This was evidenced by the nearly unchanged ethylene response in control plants. The sensor's placement at the back of the leaf allowed unrestricted light interaction with the top surface of the leaf, which was crucial for photosynthesis. Moreover, the

Authorized licensed use limited to: Iowa State University Library. Downloaded on May 12,2024 at 22:25:05 UTC from IEEE Xplore. Restrictions apply.
© 2023 IEEE. Personal use is permitted, but republication/redistribution requires IEEE permission. See https://www.ieee.org/publications/rights/index.html for more information.

This article has been accepted for publication in IEEE Sensors Journal. This is the author's version which has not been fully edited and
content may change prior to final publication. Citation information: DOI 10.1109/JSEN.2023.3327547

small footprint of the sensor ensured minimal disruption to transpiration. Notably, previous studies also report that sensor attachment to plant leaves did not cause noticeable stress on plants [23], [43], [44]. Additionally, the sticker backing of the tattoo was waterproof, protecting the sensors from rain.

Furthermore, Fig. 8f-g show the dynamic measurements of leaf relative humidity and ethylene. For this experiment, the sensors were attached to two leaves of the same bell pepper plant. The lower leaf was 40 cm above the soil, while the upper leaf was 105 cm above the soil. The plant was irrigated before commencing data collection. From Fig. 8f, it is evident that when water reached either the lower or upper leaf, an upward transition in the measured relative humidity was noted. Water reached the upper leaf from the lower leaf in about 170 minutes. Almost simultaneously, the same tattoo sensors also measured ethylene levels. The ethylene concentrations emitted from the upper leaf were greater than those released by the lower leaf (Fig. 8g). This could be attributed to the lower leaf receiving water before the upper leaf, resulting in comparatively lower stress levels for the lower leaf in contrast to the upper leaf. Additionally, two sensors were installed on the same leaf located at 75 cm above the soil surface. One sensor was placed near the base of the leaf, while the other placed near the apex. Fig. 8h shows the water dynamics in the leaf measured with the RH sensor.

The accuracy of our tattoo sensor in detecting ethylene gas emitted from plants was verified by comparing the sensor's readings against known concentrations produced by the mass flow controller. The gas sensing setup used for characterizing the ethylene sensor (explained in Section IV.C) was utilized for this purpose. The ethylene sensor demonstrated a high Pearson correlation coefficient of >0.92.

B. Monitoring Ethylene Emission in Temperature or Dark Stressed Plants

The plants were subjected to alternating cycles of cold and heat stresses. Fig. 9a-c demonstrate the dynamics of ethylene concentrations measured with the tattoo sensor. All experiments were conducted with five bell pepper plants. The gray bars depict dark periods, while the white bars represent light periods. The room temperature was close to 25 ºC. Firstly, when the leaves were heated to 50 ºC, the ethylene concentration elevated by 4 ppm in 12 hours, as illustrated in Fig. 9a. Similar results were observed during subsequent heating cycles. However, following the first heat stress cycle (i.e., 25 ºC → 50 ºC → 25 ºC), the ethylene concentration did not return to its original baseline value of ~8 ppm. This phenomenon could be attributed to the plants already being stressed due to the heat application, and the subsequent cooling down to room temperature did not entirely reverse the stress condition. A similar phenomenon was observed when the plants were subjected to cold stress cycles (Fig. 9b) and alternating cycles of cold and heat stresses (Fig. 9c).

The plants were also exposed to dark stress conditions by placing them in a dark room for 24 hours, followed by 12 hours of exposure to sunlight, and then another 24 hours of darkness, as shown in Fig. 9d. The first 12 hours of darkness was corresponded to nighttime. As the plants followed their natural diurnal cycle, there was no added stress, resulting in a decrease in ethylene concentration. However, when the plants were subjected to darkness for an additional 12 hours, they were deprived from light and ethylene levels continued to rise. From the 24th to the 48th hour, the plants underwent another diurnal cycle, leading to a subsequent decrease in ethylene levels. Afterward, the plants were subjected to 12 hours of dark stress, causing an increase in the ethylene concentration.

During both temperature and dark stress experiments, the ethylene levels did not revert back to the initial baseline value once the stress was removed, indicating an irreversible physiological alteration in the plants.

C. Monitoring Ethylene Emission from Plants under Combined Stressors

In a separate experiment, the plants were subjected to multiple abiotic stressors simultaneously. The data presented in Fig. 9g were collected subsequent to the heat stress experiment depicted in Fig. 9a. This explains why the initial ethylene level in Fig. 9g is about 14 ppm. Furthermore, interesting phenomena was observed when the plants were exposed to multiple stressors. As illustrated in Fig. 9e-g, the rate of rise in the ethylene concentration was slower compared to the rate at which ethylene increase was triggered by a single stress factor (Fig. 9a-d). An analogous finding was reported in [44], where, after an extended period of light stress, there was no substantial change in the plant's glucose level. This phenomenon can be interpreted in various ways. One potential explanation is related to stomatal closure. Research findings in

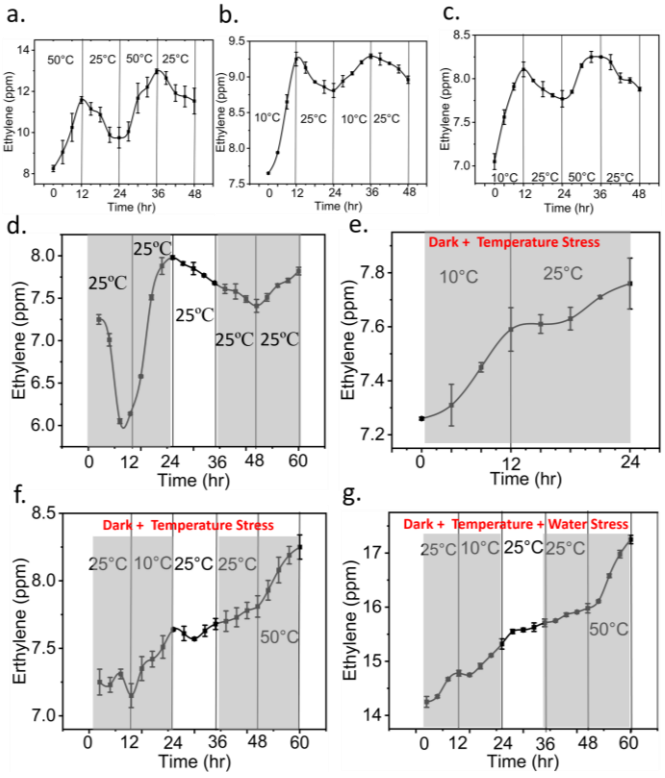

Fig. 9. Ethylene concentration dynamics monitored with the tattoo sensor when the plant was subjected to (a) heat stress cycles, (b) cold stress cycles, (c) alternating cold and heat stress cycles, (d) dark stress cycles, (e) combined dark and cold stress cycles, (f) combined light and cold/heat stress cycles, and (g) combined dark, cold/heat and water stress cycles. All experiments were conducted with five plants, with error bars indicating plant-to-plant standard errors. The dark periods are depicted by the gray bars, while the light periods are represented by the white bars.

Authorized licensed use limited to: Iowa State University Library. Downloaded on May 12,2024 at 22:25:05 UTC from IEEE Xplore. Restrictions apply.
© 2023 IEEE. Personal use is permitted, but republication/redistribution requires IEEE permission. See https://www.ieee.org/publications/rights/index.html for more information.

This article has been accepted for publication in IEEE Sensors Journal. This is the author's version which has not been fully edited and
content may change prior to final publication. Citation information: DOI 10.1109/JSEN.2023.3327547

the literature suggest that prolonged stress leads to the closure of stomata as a protective mechanism in plants to reduce water loss through transpiration [41], [45]. In this way, the stressed plant can conserve its resources in the event of a stress. When multiple stressors are present, the rate and duration of stomatal closure might be intensified compared to the effects of a single stressor. Consequently, the emission of ethylene through stomatal openings is reduced. Another possible explanation involves complex interactions between different stress pathways and hormonal responses within the plant [46]. The plant's ability to allocate resources and prioritize its stress responses can impact the overall ethylene production. Under certain circumstances, the combined stressors may trigger a synergistic effect, causing an increased ethylene production, while in other instances, the effect may be antagonistic which can modulate the ethylene production differently [47], [48]. The plant's response to combined stressors is a complex area of research and can vary based on various factors including the type, duration, and intensity of stressors, the plant genotype, and the developmental stage of the plant [49]. In the future, we plan to investigate the interactions between stress and ethylene production pathways in plants. The tattoo sensor presented in this work has the potential to elucidate these pathways in real-time and sprout new avenues for research in this field. The exploration of such details in real-time has been hindered in the past due to the absence of a wearable plant sensing technology.

D. Statistical Analysis

Statistical analysis was performed using the t-test to find the statistically significant difference (represented by the p value) in the measured ethylene concentrations in response to different stresses. Fig. 10 shows the p values computed for different combinations of stressors. The results in Fig. 10a show a statistically significant difference between the ethylene concentrations emitted from the unstressed plant (kept at 25 ºC) and cold stressed plant (at 10 ºC), denoted by p = 0.0462 (i.e., < 0.05). Likewise, the ethylene concentrations emitted from the unstressed plant (kept at 25 ºC) and heat stressed plant (at 50 ºC) represent p = 0.008. There was a statistically significant difference between ethylene released from heat stressed and dark stressed plants (p = 0.0105). Fig. 10b shows the p values between different combinations of combined stressors. In all the cases, the p value remains below 0.01, indicating a high significant difference between the stress conditions.

VI. Performance Comparison

Only a limited number of electrochemical ethylene sensors have been documented in the literature. Table II shows the primary electrochemistry-based ethylene sensors from the literature. None of them are designed to monitor ethylene emissions from plants. To the best of our knowledge, our research group is the first to report a plant-wearable sensor that can measure and monitor a plant hormone *in situ* [23]. The tattoo-like sensor presented in this work is an improved version of our prior work. The inclusion of a chemiresistive copper cofactor-coated sensor in the tattoo design eliminates the need for a solid-state electrolyte or substrate, enabling the

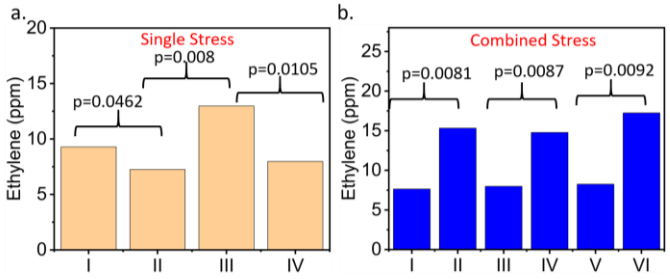

Fig. 10. (a) Ethylene response under single stress conditions. Here, I = cold stress at 10 ºC, II = room temperature condition at 25 ºC, III = heat stress at 50 ºC, and IV = dark stress for 12 hours at 25 ºC. (b) Ethylene response under combined stress conditions. Here, I = dark stress for 12 hours coupled with cold stress at 10 ºC, II = dark stress for 12 hours coupled with cold stress at 10 ºC and water stress, III = dark stress for 12 hours at 25 ºC, IV = dark stress for 12 hours at 25 ºC coupled with water stress, V = dark stress for 12 hours coupled with heat stress at 50 ºC, and VI = dark stress for 12 hours coupled with heat stress at 50 ºC and water stress.

integration of multiple sensors on a single platform. Moreover, the tattoo framework allows easy attachment and removal of the sensor resembling a scotch tape, along with extended operational capability even in adverse environmental conditions like rain and hail. Although the sensor developed by Fong et al. [50] exhibits a lower detection limit compared to our sensor, their linear operation range is limited to 50 ppm of ethylene, whereas our sensor maintains a linear response up to 115 ppm. Moreover, our sensor offers flexibility, multiplexing capability, and plant wearability, which are absent in [50]. Our sensors demonstrates superior detection limit [24]–[26] and linear operation range [25], [26], [50] compared to other electrochemical ethylene sensors reported in the literature and outlined in Table II.

TABLE II
Performance Comparison of Ethylene Sensors

Sensing Material and substrate	Sensitivity	Limit of Detection	Linear Range	Ref.
$[PdCl_2(PhCN)_2]$ and $^nBu_4N[NO_2]$ on glass	1.2%/ppm	0.015 ppm	500 ppb–50 ppm	[50]
1-butyl 3-methylimidazolium bis(trifluoromethylsulfonyl)imide [BMIM][NTf_2] immobilized in a poly(vinylidene fluoride) matrix deposited on ceramic and Kapton substrates	1.164 nA/ppm on ceramic 0.14 nA/ppm on Kapton	0.8 ppm	0 – 500 ppm	[24]
[BMIM][NTf_2] and 1-hexyl-3-methylimidazolium tris(pentafluoroethyl) trifluorophosphate [HMIM][FAP] ionic liquids on a dual in-line package	51 pA/ppm	0.76 ppm	0 – 10 ppm	[25]
Copper complex and SWCNT conjugate on a glass slide	0.038%/ppm	0.5 ppm	0.5 – 50 ppm	[26]
Copper complex and SWCNT conjugate on tattoo paper	0.6295 kΩ/ppm	0.13 ppm	0.1 – 115 ppm	This work

Authorized licensed use limited to: Iowa State University Library. Downloaded on May 12,2024 at 22:25:05 UTC from IEEE Xplore. Restrictions apply.
© 2023 IEEE. Personal use is permitted, but republication/redistribution requires IEEE permission. See https://www.ieee.org/publications/rights/index.html for more information.

This article has been accepted for publication in IEEE Sensors Journal. This is the author's version which has not been fully edited and
content may change prior to final publication. Citation information: DOI 10.1109/JSEN.2023.3327547

VII. Conclusion

In summary, this work presents a tattoo sensor for the first time for real-time monitoring of ethylene emissions from live plants. The sensor operates based on chemiresistive principles and features a coating composed of copper complex and SWCNT that offers high sensitivity and reversibility. The ethylene readings were corrected to account for the influence of leaf temperature and humidity on the recorded ethylene measurements. To accomplish this, temperature and humidity sensors were incorporated on the same tattoo substrate. The entire tattoo can be effortlessly affixed to the leaves just like using a scotch tape. Measurements of ethylene were collected from plants exposed to individual stressors like water deficiency, low temperatures, high temperatures, and dark stress, as well as from plants subjected to combined stress conditions like the combination of temperature and dark stress, and the combination of temperature, dark, and water stress. A notable statistical significance, marked by $p<0.05$, was identified between different stress types. Scaling up the fabrication of these tattoos through roll-to-roll processes will facilitate their widespread utilization in agricultural fields.

Acknowledgment

The authors thank the applications specialists from Jeol, Inc., USA for conducting SEM imaging of the sensors.

References

[1] C. S. Barry and J. J. Giovannoni, "Ethylene and Fruit Ripening," *J Plant Growth Regul*, vol. 26, no. 2, pp. 143–159, Jun. 2007, doi: 10.1007/s00344-007-9002-y.

[2] M. Liu *et al.*, "The chimeric repressor version of an Ethylene Response Factor (ERF) family member, Sl-ERF.B3, shows contrasting effects on tomato fruit ripening," *New Phytol*, vol. 203, no. 1, pp. 206–218, Jul. 2014, doi: 10.1111/nph.12771.

[3] H. J. Klee and J. J. Giovannoni, "Genetics and control of tomato fruit ripening and quality attributes," *Annu Rev Genet*, vol. 45, pp. 41–59, 2011, doi: 10.1146/annurev-genet-110410-132507.

[4] P. Achard *et al.*, "Integration of Plant Responses to Environmentally Activated Phytohormonal Signals," *Science*, vol. 311, no. 5757, pp. 91–94, Jan. 2006, doi: 10.1126/science.1118642.

[5] N. Beaudoin, C. Serizet, F. Gosti, and J. Giraudat, "Interactions between abscisic acid and ethylene signaling cascades," *Plant Cell*, vol. 12, no. 7, pp. 1103–1115, Jul. 2000, doi: 10.1105/tpc.12.7.1103.

[6] L. C. van Loon, B. P. J. Geraats, and H. J. M. Linthorst, "Ethylene as a modulator of disease resistance in plants," *Trends Plant Sci*, vol. 11, no. 4, pp. 184–191, Apr. 2006, doi: 10.1016/j.tplants.2006.02.005.

[7] R. P. Savada, J. A. Ozga, C. P. A. Jayasinghege, K. D. Waduthanthri, and D. M. Reinecke, "Heat stress differentially modifies ethylene biosynthesis and signaling in pea floral and fruit tissues," *Plant Mol Biol*, vol. 95, no. 3, pp. 313–331, Oct. 2017, doi: 10.1007/s11103-017-0653-1.

[8] M. Dubois, H. Claeys, L. Van den Broeck, and D. Inzé, "Time of day determines Arabidopsis transcriptome and growth dynamics under mild drought," *Plant Cell Environ*, vol. 40, no. 2, pp. 180–189, Feb. 2017, doi: 10.1111/pce.12809.

[9] A. Skirycz *et al.*, "Pause-and-stop: the effects of osmotic stress on cell proliferation during early leaf development in Arabidopsis and a role for ethylene signaling in cell cycle arrest," *Plant Cell*, vol. 23, no. 5, pp. 1876–1888, May 2011, doi: 10.1105/tpc.111.084160.

[10] U. Druege, "Ethylene and Plant Responses to Abiotic Stress," in *Ethylene Action in Plants*, N. A. Khan, Ed., Berlin, Heidelberg: Springer, 2006, pp. 81–118. doi: 10.1007/978-3-540-32846-9_5.

[11] S. Giannarelli, B. Muscatello, P. Bogani, M. M. Spiriti, M. Buiatti, and R. Fuoco, "Comparative determination of some phytohormones in wild-type and genetically modified plants by gas chromatography-mass spectrometry and high-performance liquid chromatography-tandem mass spectrometry," *Anal Biochem*, vol. 398, no. 1, pp. 60–68, Mar. 2010, doi: 10.1016/j.ab.2009.10.038.

[12] "AN034: Simultaneous soil flux measurements of five gases - N2O, CH4, CO2, NH3 and H2O - G2508 | Picarro." Accessed: Aug. 26, 2023. [Online]. Available: https://www.picarro.com/support/library/documents/an034_simultaneous_soil_flux_measurements_of_five_gases_n2o_ch4_co2_nh3

[13] F. Wiß *et al.*, "Net ecosystem fluxes and composition of biogenic volatile organic compounds over a maize field–interaction of meteorology and phenological stages," *GCB Bioenergy*, vol. 9, no. 11, pp. 1627–1643, 2017, doi: 10.1111/gcbb.12454.

[14] F. Havermann *et al.*, "Modeling Intra- and Interannual Variability of BVOC Emissions From Maize, Oil-Seed Rape, and Ryegrass," *Journal of Advances in Modeling Earth Systems*, vol. 14, p. e2021MS002683, Mar. 2022, doi: 10.1029/2021MS002683.

[15] N. Copeland, J. N. Cape, and M. R. Heal, "Volatile organic compound emissions from Miscanthus and short rotation coppice willow bioenergy crops," *Atmospheric Environment*, vol. 60, pp. 327–335, Dec. 2012, doi: 10.1016/j.atmosenv.2012.06.065.

[16] M. Graus *et al.*, "Biosphere-atmosphere exchange of volatile organic compounds over C4 biofuel crops," *Atmospheric Environment*, vol. 66, pp. 161–168, Feb. 2013, doi: 10.1016/j.atmosenv.2011.12.042.

[17] A. Galieni, N. D'Ascenzo, F. Stagnari, G. Pagnani, Q. Xie, and M. Pisante, "Past and Future of Plant Stress Detection: An Overview From Remote Sensing to Positron Emission Tomography," *Front Plant Sci*, vol. 11, p. 609155, 2020, doi: 10.3389/fpls.2020.609155.

[18] Z. Zhang, J. Boubin, C. Stewart, and S. Khanal, "Whole-Field Reinforcement Learning: A Fully Autonomous Aerial Scouting Method for Precision Agriculture," *Sensors*, vol. 20, no. 22, Art. no. 22, Jan. 2020, doi: 10.3390/s20226585.

[19] J. del Cerro, C. Cruz Ulloa, A. Barrientos, and J. de León Rivas, "Unmanned Aerial Vehicles in Agriculture: A Survey," *Agronomy*, vol. 11, no. 2, Art. no. 2, Feb. 2021, doi: 10.3390/agronomy11020203.

[20] T. Dutta, T. Noushin, S. Tabassum, and S. K. Mishra, "Road Map of Semiconductor Metal-Oxide-Based Sensors: A Review," *Sensors*, vol. 23, no. 15, Art. no. 15, Jan. 2023, doi: 10.3390/s23156849.

[21] S. Tabassum, D. P. Kumar, and R. Kumar, "Copper Complex-Coated Nanopatterned Fiber-Tip Guided Mode Resonance Device for Selective Detection of Ethylene," *IEEE Sensors Journal*, vol. 21, no. 16, pp. 17420–17429, Aug. 2021, doi: 10.1109/JSEN.2021.3057619.

[22] E. E. G. Martínez, M. H. Otamendi, C. R. Zamarreño, and I. R. Matías, "LMR-Based Optical Sensor for Ethylene Detection at Visible and Mid-Infrared Regions," *IEEE Sensors Letters*, vol. 7, no. 8, pp. 1–4, Aug. 2023, doi: 10.1109/LSENS.2023.3297371.

[23] N. I. Hossain and S. Tabassum, "A hybrid multifunctional physicochemical sensor suite for continuous monitoring of crop health," *Sci Rep*, vol. 13, no. 1, Art. no. 1, Jun. 2023, doi: 10.1038/s41598-023-37041-z.

[24] P. Kuberský, J. Navrátil, T. Syrový, P. Sedlák, S. Nešpůrek, and A. Hamáček, "An Electrochemical Amperometric Ethylene Sensor with Solid Polymer Electrolyte Based on Ionic Liquid," *Sensors (Basel)*, vol. 21, no. 3, p. 711, Jan. 2021, doi: 10.3390/s21030711.

[25] M. A. G. Zevenbergen, D. Wouters, V.-A. T. Dam, S. H. Brongersma, and M. Crego-Calama, "Electrochemical Sensing of Ethylene Employing a Thin Ionic-Liquid Layer," *Anal. Chem.*, vol. 83, no. 16, pp. 6300–6307, Aug. 2011, doi: 10.1021/ac2009756.

[26] B. Esser, J. M. Schnorr, and T. M. Swager, "Selective detection of ethylene gas using carbon nanotube-based devices: utility in determination of fruit ripeness," *Angew Chem Int Ed Engl*, vol. 51, no. 23, pp. 5752–5756, Jun. 2012, doi: 10.1002/anie.201201042.

[27] K. H. Jensen and B. W. Michel, "Detection of Ethylene with Defined Metal Complexes: Strategies and Recent Advances," *Analysis & Sensing*, vol. 3, no. 2, p. e202200058, 2023, doi: 10.1002/anse.202200058.

[28] J. R. Bautista-Quijano, P. Pötschke, H. Brünig, and G. Heinrich, "Strain sensing, electrical and mechanical properties of polycarbonate/multiwall carbon nanotube monofilament fibers fabricated by melt spinning," *Polymer*, vol. 82, pp. 181–189, Jan. 2016, doi: 10.1016/j.polymer.2015.11.030.

[29] E. Bilotti, R. Zhang, H. Deng, M. Baxendale, and T. Peijs, "Fabrication and property prediction of conductive and strain sensing TPU/CNT nanocomposite fibres," *J. Mater. Chem.*, vol. 20, no. 42, pp. 9449–9455, Oct. 2010, doi: 10.1039/C0JM01827A.

[30] T. Noushin and S. Tabassum, "Kirigami-shaped Dual-functional Strain and Temperature Sensors for Monitoring Body Movements and

Authorized licensed use limited to: Iowa State University Library. Downloaded on May 12,2024 at 22:25:05 UTC from IEEE Xplore. Restrictions apply.
© 2023 IEEE. Personal use is permitted, but republication/redistribution requires IEEE permission. See https://www.ieee.org/publications/rights/index.html for more information.

This article has been accepted for publication in IEEE Sensors Journal. This is the author's version which has not been fully edited and content may change prior to final publication. Citation information: DOI 10.1109/JSEN.2023.3327547

Hyperthermia Toward Physiotherapy Applications," *IEEE Sensors Journal*, pp. 1–1, 2023, doi: 10.1109/JSEN.2023.3272622.

[31] S. M. Vemuru, R. Wahi, S. Nagarajaiah, and P. M. Ajayan, "Strain sensing using a multiwalled carbon nanotube film," *The Journal of Strain Analysis for Engineering Design*, vol. 44, no. 7, pp. 555–562, Oct. 2009, doi: 10.1243/03093247JSA535.

[32] T. Noushin, N. I. Hossain, and S. Tabassum, "IoT-Enabled Integrated Smart Wound Sensor for Multiplexed Monitoring of Inflammatory Biomarkers at the Wound Site," *Frontiers in Nanotechnology*, vol. 4, 2022, Accessed: Dec. 18, 2022. [Online]. Available: https://www.frontiersin.org/articles/10.3389/fnano.2022.851041

[33] J. Turkevich, P. C. Stevenson, and J. Hillier, "A study of the nucleation and growth processes in the synthesis of colloidal gold," *Discuss. Faraday Soc.*, vol. 11, no. 0, pp. 55–75, Jan. 1951, doi: 10.1039/DF9511100055.

[34] S. Rahmam, N. M. Mohamed, and S. Sufian, "Effect of acid treatment on the multiwalled carbon nanotubes," *Materials Research Innovations*, vol. 18, no. sup6, pp. S6-196-S6-199, 2014, doi: 10.1179/1432891714Z.0000000001038.

[35] A. G. Osorio, I. C. L. Silveira, V. L. Bueno, and C. P. Bergmann, "H2SO4/HNO3/HCl—Functionalization and its effect on dispersion of carbon nanotubes in aqueous media," *Applied Surface Science*, vol. 255, no. 5, Part 1, pp. 2485–2489, Dec. 2008, doi: 10.1016/j.apsusc.2008.07.144.

[36] W. Wang, J. Wang, Y. Kang, and A. Wang, "Synthesis, swelling and responsive properties of a new composite hydrogel based on hydroxyethyl cellulose and medicinal stone," *Composites Part B: Engineering*, vol. 42, no. 4, pp. 809–818, Jun. 2011, doi: 10.1016/j.compositesb.2011.01.018.

[37] A. Thamri, H. Baccar, C. Struzzi, C. Bittencourt, A. Abdelghani, and E. Llobet, "MHDA-Functionalized Multiwall Carbon Nanotubes for detecting non-aromatic VOCs," *Sci Rep*, vol. 6, no. 1, Art. no. 1, Oct. 2016, doi: 10.1038/srep35130.

[38] S. Kundu, S. Tabassum, and R. Kumar, "Plasmonic Point-of-Care Device for Sepsis Biomarker Detection," *IEEE Sensors Journal*, vol. 21, no. 17, pp. 18837–18846, Sep. 2021, doi: 10.1109/JSEN.2021.3088117.

[39] A. Wiorek, M. Parrilla, M. Cuartero, and G. A. Crespo, "Epidermal Patch with Glucose Biosensor: pH and Temperature Correction toward More Accurate Sweat Analysis during Sport Practice," *Anal. Chem.*, vol. 92, no. 14, pp. 10153–10161, Jul. 2020, doi: 10.1021/acs.analchem.0c02211.

[40] N. S. Nise, *Control Systems Engineering*, 6th Edition Binder Ready Version. Hoboken, NJ: Wiley, 2010.

[41] M. Melotto, W. Underwood, and S. Y. He, "Role of Stomata in Plant Innate Immunity and Foliar Bacterial Diseases," *Annu Rev Phytopathol*, vol. 46, pp. 101–122, 2008, doi: 10.1146/annurev.phyto.121107.104959.

[42] S. Assouline and D. Or, "Plant Water Use Efficiency over Geological Time – Evolution of Leaf Stomata Configurations Affecting Plant Gas Exchange," *PLOS ONE*, vol. 8, no. 7, p. e67757, Jul. 2013, doi: 10.1371/journal.pone.0067757.

[43] G. Lee *et al.*, "Abaxial leaf surface-mounted multimodal wearable sensor for continuous plant physiology monitoring," *Science Advances*, vol. 9, no. 15, p. eade2232, Apr. 2023, doi: 10.1126/sciadv.ade2232.

[44] S. A. Perdomo *et al.*, "Non-invasive in-vivo glucose-based stress monitoring in plants," *Biosensors and Bioelectronics*, vol. 231, p. 115300, Jul. 2023, doi: 10.1016/j.bios.2023.115300.

[45] M. Melotto, L. Zhang, P. R. Oblessuc, and S. Y. He, "Stomatal Defense a Decade Later1[OPEN]," *Plant Physiol*, vol. 174, no. 2, pp. 561–571, Jun. 2017, doi: 10.1104/pp.16.01853.

[46] M. Fatma *et al.*, "Ethylene Signaling under Stressful Environments: Analyzing Collaborative Knowledge," *Plants (Basel)*, vol. 11, no. 17, p. 2211, Aug. 2022, doi: 10.3390/plants11172211.

[47] I. Ben Rejeb, V. Pastor, and B. Mauch-Mani, "Plant Responses to Simultaneous Biotic and Abiotic Stress: Molecular Mechanisms," *Plants (Basel)*, vol. 3, no. 4, pp. 458–475, Oct. 2014, doi: 10.3390/plants3040458.

[48] D. T. Teshome, G. E. Zharare, and S. Naidoo, "The Threat of the Combined Effect of Biotic and Abiotic Stress Factors in Forestry Under a Changing Climate," *Frontiers in Plant Science*, vol. 11, 2020, Accessed: Aug. 30, 2023. [Online]. Available: https://www.frontiersin.org/articles/10.3389/fpls.2020.601009

[49] L. Mareri, L. Parrotta, and G. Cai, "Environmental Stress and Plants," *Int J Mol Sci*, vol. 23, no. 10, p. 5416, May 2022, doi: 10.3390/ijms23105416.

[50] D. Fong, S.-X. L. Luo, R. S. Andre, and T. M. Swager, "Trace Ethylene Sensing via Wacker Oxidation," *ACS Cent. Sci.*, vol. 6, no. 4, pp. 507–512, Apr. 2020, doi: 10.1021/acscentsci.0c00022.

Nafize I. Hossain received his B.Sc. degree in Electrical and Electronic Engineering from Chittagong University of Engineering and Technology (CUET), Bangladesh in 2016 and his M.S. in Electrical Engineering from the University of Texas at Tyler, Tyler, TX, USA in 2022. From 2016 to 2019, he was an R&D Engineer at Walton Micro-Tech Corporation, where he worked on television motherboard and operating system development, as well as television production process development.

Currently, he is pursuing his Ph.D. Degree in Electrical and Computer Engineering at Tufts University, MA, USA. His research focuses on developing flexible, wearable, electrochemical sensors with applications in healthcare and precision agriculture. He was the recipient of IEEE NEMS Best Student Paper award, Bridge Venture Fellowship, and Outstanding Graduate Student of the year in 2022.

Tanzila Noushin completed her B.Sc. in Electrical and Electronics Engineering from Rajshahi University of Engineering and Technology (RUET), Bangladesh in 2016 and her M.S. in Electrical Engineering from the University of Texas at Tyler, Tyler, TX, USA in 2022.

Currently, she is pursuing her Ph.D. Degree in Electrical and Computer Engineering at the University of Texas at Dallas, TX, USA. Her research interests include developing flexible and wearable sensors for biomedical applications. She has won several awards including UT Tyler's 3-minute thesis competition, student employee leadership award, and third place at big idea pitch competition in 2022 and 2021, respectively.

Dr. Shawana Tabassum is an Assistant Professor of Electrical Engineering at the University of Texas at Tyler, Tyler, TX, USA, where she directs the Biosensors and Bioinformatics Laboratory. Her research focuses on the development of flexible, soft, and micro/nano-structured optical and electrochemical sensors and actuators for biomedicine, and sustainable and precision agriculture. She received her B.Sc. degree in Electrical Engineering from Bangladesh University of Engineering and Technology, Bangladesh, and her Ph.D. degree in electrical and computer engineering from Iowa State University (ISU), Ames, IA, USA, in 2014 and 2018, respectively. From 2018 to 2020, she was a Postdoctoral Research Associate at Iowa State University.

Dr. Tabassum's notable awards and honors include Curtis W. McGraw Research Award (2023), Mary John and Ralph Spence Professorship (2023), Dean's Award for Excellence in Research and Scholarship (2022), American Association of University Women's Research Publication grant (2022), Science Breakthrough of the Year: Emerging Talent from the Falling Walls Lab Berlin global finale (2020), Robert J. Menges award for outstanding research in educational development (2020), Postdoctoral Scholar Excellence award for teaching and mentoring students (2020), Best global impact innovation prize from ISU's Pappajohn Center for Entrepreneurship (2020, 2019), Biomedical Engineering Society's career development award (2019), ISU's Research Excellence Award (2018), and the Best paper award finalist at IEEE Sensors conference (2016).

Authorized licensed use limited to: Iowa State University Library. Downloaded on May 12,2024 at 22:25:05 UTC from IEEE Xplore. Restrictions apply.
© 2023 IEEE. Personal use is permitted, but republication/redistribution requires IEEE permission. See https://www.ieee.org/publications/rights/index.html for more information.